The complex organic molecular content in the L1498 starless Core

Jiménez-Serra, I.; Vasyunin, A.I.; Spezzano, S.; Caselli, P.; Cosentino, G.; Viti, S.

Citation

Jiménez-Serra, I., Vasyunin, A. I., Spezzano, S., Caselli, P., Cosentino, G., & Viti, S. (2021). The complex organic molecular content in the L1498 starless Core. *The Astrophysical Journal*, *917*(1). doi:10.3847/1538-4357/ac024c

Version: Not Applicable (or Unknown)
License: Leiden University Non-exclusive license
Downloaded from: https://hdl.handle.net/1887/3256742

Note: To cite this publication please use the final published version (if applicable).

Draft version May 19, 2021
Typeset using LATEX **preprint2** style in AASTeX63

arXiv:2105.08363v1 [astro-ph.SR] 18 May 2021

The complex organic molecular content in the L1498 starless core

Izaskun Jiménez-Serra,[1] Anton I. Vasyunin,[2] Silvia Spezzano,[3] Paola Caselli,[3]
Giuliana Cosentino,[4] and Serena Viti[5]

[1]*Centro de Astrobiología (CSIC-INTA), Ctra. de Torrejón a Ajalvir km 4, 28850, Torrejón de Ardoz, Spain*
[2]*Ural Federal University, Kuybysheva st. 48, 620002, Ekaterinburg, Russian Federation*
[3]*Max Planck Institute for Extraterrestrial Physics, Giessenbachstrasse 1, 85748, Garching, Germany*
[4]*Chalmers University of Technology, SE41296, Gothenburg, Sweden*
[5]*University of Leiden, Niels Bohrweg 2, 2333 CA, Leiden, The Netherlands*

(Received June 1, 2019; Revised January 10, 2019; Accepted May 19, 2021)

Submitted to ApJ

ABSTRACT

Observations carried out toward starless and pre-stellar cores have revealed that complex organic molecules are prevalent in these objects, but it is unclear what chemical processes are involved in their formation. Recently, it has been shown that complex organics are preferentially produced at an intermediate-density shell within the L1544 pre-stellar core at radial distances of ∼4000 au with respect to the core center. However, the spatial distribution of complex organics has only been inferred toward this core and it remains unknown whether these species present a similar behaviour in other cores. We report high-sensitivity observations carried out toward two positions in the L1498 pre-stellar core, the dust peak and a position located at a distance of ∼11000 au from the center of the core where the emission of CH_3OH peaks. Similarly to L1544, our observations reveal that small O-bearing molecules and N-bearing species are enhanced by factors ∼4-14 toward the outer shell of L1498. However, unlike L1544, large O-bearing organics such as CH_3CHO, CH_3OCH_3 or CH_3OCHO are not detected within our sensitivity limits. For N-bearing organics, these species are more abundant toward the outer shell of the L1498 pre-stellar core than toward the one in L1544. We propose that the differences observed between O-bearing and N-bearing species in L1498 and L1544 are due to the different physical structure of these cores, which in turn is a consequence of their evolutionary stage, with L1498 being younger than L1544.

Keywords: Interstellar medium (847) — Interstellar molecules (849) — Astrochemistry (75) — Molecular clouds (1072)

1. INTRODUCTION

Complex Organic Molecules (or COMs) are defined in Astrochemistry as carbon-bearing compounds with at least 6 atoms in their struc-

Corresponding author: Izaskun Jiménez-Serra
ijimenez@cab.inta-csic.es

ture (Herbst & van Dishoeck 2009). COMs were initially detected toward hot sources with temperatures ≥100 K such as massive hot cores (Hollis et al. 2000, 2006; Belloche et al. 2008, 2013) or low-mass warm cores (i.e. hot corinos; Bottinelli et al. 2004; Jorgensen et al. 2012). For this reason, it was first postulated that COMs only form on dust grains via hydrogenation and atom addition reactions (as for e.g. methanol; see Watanabe & Kouchi 2002; Charnley et al. 1995) or radical-radical reactions favoured by the heating from the central protostar when the temperatures get higher than 30 K (see Garrod et al. 2008). This hypothesis implied that COMs could only form via hydrogenation in the coldest environments of the ISM such as dense dark cloud cores (with T≤10 K), and that, if formed, they would not be seen in the gas phase.

In the past decade, however, there has been a number of observational works that have changed our view of COM formation in the ISM. Large COM species such as propylene (CH_2CHCH_3), acetaldehyde (CH_3CHO), dimethyl ether (CH_3OCH_3) or methyl formate (CH_3OCHO) have been found in the gas-phase toward dark cloud cores and starless/pre-stellar cores (Marcelino et al. 2007; Öberg et al. 2010; Bacmann et al. 2012; Cernicharo et al. 2012; Vastel et al. 2014; Jiménez-Serra et al. 2016; Soma et al. 2018; Agúndez et al. 2019; Yoshida et al. 2019; Scibelli & Shirley 2020). These observations have triggered a plethora of theoretical and experimental studies to understand COM formation at low temperatures (see e.g. Rawlings et al. 2013; Vasyunin & Herbst 2013; Balucani et al. 2015; Ivlev et al. 2015; Ruaud et al. 2015; Chuang et al. 2016; Quenard et al. 2018; Shingledecker et al. 2018; Holdship et al. 2019; Jin & Garrod 2020), although no consensus has been reached yet.

To gain insight into the processes involved in the formation of COMs in cold sources, Jiménez-Serra et al. (2016) measured the abundance profiles of complex organics toward the L1544 pre-stellar core by means of high-sensitivity single-dish observations. Two positions in the core were observed: the dust peak of L1544 with a visual extinction A_v≥60 mag (the core's center); and the position where CH_3OH, the most abundant COM, peaks in L1544 (*the methanol peak*; Bizzocchi et al. 2014; Spezzano et al. 2016). The latter position is representative of an outer, lower-density shell located at a radius of 4000 au from the core's center and visual extinction A_v∼15-16 mag. The high-sensitivity observations not only revealed the presence of large COMs such as CH_3OCHO, CH_3OCH_3, and CH_2CHCN in L1544 (these species had remained elusive in previous campaigns; see Vastel et al. 2014), but also that they are factors ∼2-10 more abundant toward the position of the methanol peak than toward L1544's center (Jiménez-Serra et al. 2016).

The modelling of the chemistry of O-bearing COMs in L1544 indeed predicts a peak in the radial abundance profiles of these species at a distance of ∼4000 au, coinciding with the location of the methanol peak and with the enhancement of O-bearing COMs (Vasyunin et al. 2017). The enhancement of these COMs in the lower-density shell of L1544 is driven by (Jiménez-Serra et al. 2016): i) the freezing-out of CO onto dust grains, which triggers an active grain surface chemistry; ii) the intermediate visual extinction at this shell (of ∼7-8 mag)[1], which is sufficient to prevent the UV photo-dissociation of COMs by the external in-

---

[1] Note that the visual extinction toward the methanol peak is A_v∼15-16 mag but this is along the whole line-of-sight. The abundances in the models of Vasyunin et al. (2017) are calculated as a function of radius, and therefore the visual extinction in the model has to be half that measured along the line-of-sight (i.e. A_v∼7-8 mag; see Jiménez-Serra et al. 2016).

terstellar radiation field; and iii) the moderate H_2 gas number densities within the shell, which prevent the severe depletion of O-bearing COMs onto grains. All this suggests that O-bearing COMs are preferentially formed toward the low-density shells in starless/pre-stellar cores. For N-bearing COMs, the observations of Jiménez-Serra et al. (2016) show that the abundances of these species are also enhanced toward the position of the methanol peak in L1544 by small factors (of 1.2-1.8), although the peak intensity of their lines show the opposite behaviour to those of O-bearing COMs: while the O-bearing COM emission is stronger toward the position of the methanol peak, the N-bearing COM lines are brighter toward the core's center. Unlike for O-bearing COMs, the formation mechanisms for N-bearing species in starless/pre-stellar cores remain vastly unexplored (see e.g. Fedoseev et al. 2018).

Until recently, the spatial distribution of O-bearing and N-bearing species in starless and pre-stellar cores had been studied only toward a few of these cores (e.g. in L1544, L1498 and L1517B; Tafalla et al. 2006; Bizzocchi et al. 2014; Spezzano et al. 2017). However, Scibelli & Shirley (2020) have recently observed the emission from CH_3OH and CH_3CHO toward a large sample of starless and pre-stellar cores in the Taurus molecular cloud. Their results show that not only these species are prevalent across the sample (CH_3OH is detected in 100% of the sources, while CH_3CHO is detected in 70% of them), but also that the emission of CH_3OH is extended with morphologies similar to those found toward other cores such as L1544, L1498 or L1517B[2]. However, it remains unclear whether all starless/pre-stellar cores present the same level of chemical complexity regardless of their evolutionary stage or environment (see e.g. Lattanzi et al. 2020), or whether COMs and their precursors are distributed in all cores in a similar fashion to that observed in L1544.

The L1498 starless core belongs to the Taurus molecular complex and it is located at a distance of 130 pc (Galli et al. 2019). By analysing the kinematics of the high-density gas, Tafalla et al. (2004) found that the core is accreting material from the surrounding cloud as revealed by clear infall asymmetries in the CS line profiles. However, the N_2H^+ emission does not show any infall signatures, which implies that the core itself is not undergoing gravitational collapse. Compared to pre-stellar (gravitationally-collapsing) cores such as L1544, L1498 shows a much flatter radial density distribution (Tafalla et al. 2004), and its deuterium fractionation [determined as $N(N_2D^+)/N(N_2H^+)$] is only 4%, significantly lower than that found in L1544 (∼23-25%; Crapsi et al. 2005; Redaelli et al. 2019). This lower deuterium fractionation is expected since it is the result of the lower CO depletion in L1498. Therefore, L1498 is likely at an earlier stage of evolution than L1544.

As L1544, L1498 also presents a methanol-rich shell. However, its methanol peak emission is located at distances further away from the center of the core (∼11000 au in L1498 vs. ∼4000 au in L1544; Tafalla et al. 2006)[3]. The visual extinction toward this position is also lower (A_v∼7-8 mag; see below) than toward the methanol peak in L1544 (A_v∼15-16 mag), which suggests that the behaviour of O-bearing and N-bearing COMs, and of their precursors, may be different from that found in L1544.

---

[2] Scibelli & Shirley (2020) mapped only seven cores from their sample in the Taurus molecular complex. Despite the poor angular resolution of their observations (beam of ∼1 arcmin), they find indications for chemical differentiation of CH_3OH toward all the mapped cores.

[3] Note that the L1498 core morphology is elongated and the methanol shell presents radii between values $r_{\rm min}$=7800 au and $r_{\rm max}$=13000 au.

Table 1. Frequency ranges, velocity resolution (δv) and rms noise level (rms) of our observations

Frequency (GHz)	δv (km s^{-1})	rms (mK)	
		Dust peak	CH_3OH peak
78.1-80.0	0.19	4.9	3.8
81.4-83.3	0.18	4.4	3.4
83.4-85.3	0.18	2.2	2.2
86.7-88.5	0.17	2.0	1.8
93.8-95.7	0.16	4.7	3.7
95.7-97.2	0.16	7.2	8.4
97.2-99.0	0.15	4.9	4.0
99.1-100.9	0.15	2.3	2.1
102.4-104.2	0.15	2.9	2.6
109.2-111.03	0.14	15.3	13.5

In this paper, we present deep observations of O-bearing and N-bearing COMs toward two positions in the L1498 starless core. The goal is to not only establish the level of chemical complexity in this core, but to understand the formation mechanisms of COMs in cold cores as a function of evolution. The manuscript is organised as follows. Section 2 describes the observations, while Section 3 reports the results on the analysis of the COM and COM precursor emission for their excitation, column densities and molecular abundances. Section 4 compares the abundances of the COMs and precursors measured toward L1498 with those obtained toward L1544. In Section 5, we model the chemistry of the observed COMs and precursors, and compare the model predictions with the observations. Finally, in Section 6, we summarise our conclusions.

2. OBSERVATIONS

The observations of the L1498 pre-stellar core were carried out at 3 mm with the Instituto de Radioastronomía Milimétrica (IRAM) 30 m telescope (Granada, Spain) between 15-17 March 2017 and 20-22 May 2017 (project number 094-16). Two positions were observed toward the L1498 core (see Figure 1): the dust continuum peak, with coordinates α(J2000)=04^{h}10^{m}53.70^s, δ(J2000)=25°10′18.0”, and the position in the L1498 core where CH_3OH shows its peak emission, α(J2000)=04^{h}10^{m}56.95^s, δ(J2000)=25°09′07.9”. The latter position (hereafter, the *methanol peak*) is indicated with a cross in Figure 1 (left panel) and it is located ∼83” away (or ∼11000 au at a distance of 130 pc) from L1498's dust peak (shown as a star in the same panel). Similarly to what is seen toward the L1544 pre-stellar core, L1498's methanol peak appears towards a high-density tail associated with the core (Figure 1). However, the ring-like methanol structure detected toward L1498 is more homogeneous than that observed toward L1544 (Figure 1 and Bizzocchi et al. 2014; Tafalla et al. 2006). Note, however, that the methanol peak in L1544 (Figure 1, right panel) is found at shorter radial distances (∼4000 au) that those associated with the methanol peak in L1498 (∼11000 au; left panel of Figure 1).

The high-sensitivity 3 mm spectra were obtained in frequency-switching mode using a frequency throw of 7.14 MHz. The EMIR E090 receivers were tuned at 84.37 GHz, 94.82 GHz and 110.16 GHz with rejections ≤10 dB. The observed frequency ranges are shown in Table 1. To avoid weak spurious features in the observed spectra, we carried out part of the observations by shifting slightly the central frequencies by ±20 MHz (see also Jiménez-Serra et al. 2016). We used the narrow mode of the FTS spectrometer that provided a spectral resolution of 50 kHz, equivalent to 0.15-0.18 km s^{-1} at 3 mm. Typical system temperatures ranged between 75-110 K and the telescope beam size was ∼24”-31” between 79 and 101 GHz. The spectra

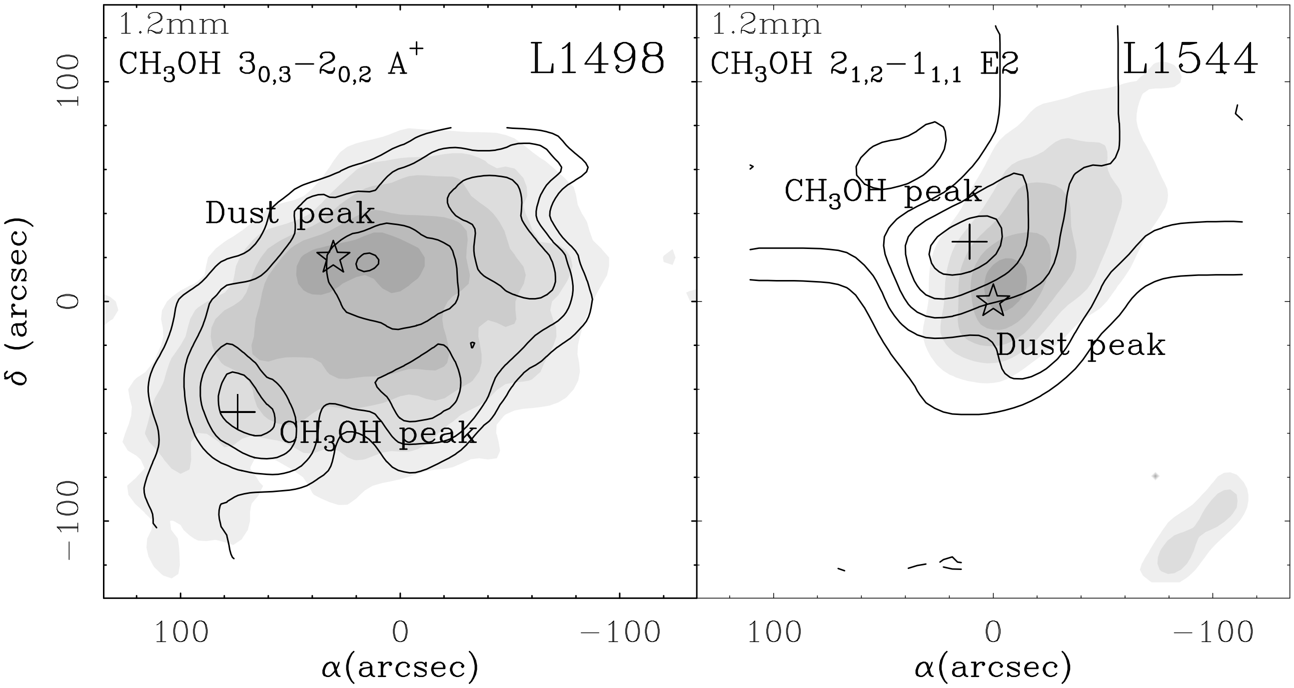

Figure 1. CH_3OH line integrated intensity maps (black contours) overlaid on the 1.2 mm dust continuum maps (grey scale) obtained toward the L1498 (left panel) and L1544 (right panel) cold cores (from Tafalla et al. 2004, 2006; Caselli et al. 2002; Spezzano et al. 2017). The grey scale indicates different percentage levels (15%, 30%, 45%, 60%, 75% and 90%) with respect to the 1.2 mm dust continuum peak flux measured toward these cores (19.4 mJy/beam for L1498 and 224.8 mJy/beam for L1544). Contours correspond to the integrated intensity levels of 0.08, 0.12, 0.16 and 0.20 $K\,km\,s^{-1}$ for the CH_3OH $3_{0,3}\rightarrow2_{0,2}$ A^+ in L1498, and to levels of 0.11, 0.19, 0.27, 0.35, and 0.43 $K\,km\,s^{-1}$ for the CH_3OH $2_{1,2}\rightarrow1_{1,1}$ E2 in L1544. Stars indicate the location of the dust peaks in both cores while crosses show the coordinates of their methanol peaks. Note that the CH_3OH peak in L1544 is found at shorter radial distances (∼4000 au) than those associated with the CH_3OH peak in L1498 (∼11000 au).

were calibrated in units of antenna temperature, T^*_A, and converted into main beam temperature, T_{mb}, by using a beam efficiency of 0.81 at 79-101 GHz and of 0.78 at 102-111 GHz. The rms noise level ranged between ∼2-15 mK for the core's center position and between ∼1.8-14 mK for the methanol peak (see Table 1). The rms noise level for the frequencies between 95.7-97.2 and 109.2-111.03 were higher than for the rest of frequency ranges because they were sufficient to detect the observed CH_3OH and CH_3CN lines with high signal-to-noise ratios.

3. RESULTS

3.1. *COMs and COM precursors spectra*

Table 2 presents the COMs and COM precursor molecules observed toward the dust and methanol peaks of L1498, along with their measured transitions, derived line parameters and signal-to-noise ratio in integrated intensity (S/N). The identification of the lines has been carried out using the SLIM (Spectral Line Identification and Modelling) tool within the MADCUBA package[4] (Martín et al. 2019). The spectroscopic entries are taken from the Cologne Database for Molecular Spectroscopy (CDMS; Endres et al. 2016) and the Jet Propulsion Laboratory (JPL; Pickett et al. 1998).

Our observations have covered both O-bearing and N-bearing COMs and COM

[4] Madrid Data Cube Analysis on ImageJ is a software developed at the Center of Astrobiology (CAB) in Madrid; http://cab.intacsic.es/madcuba/Portada.html

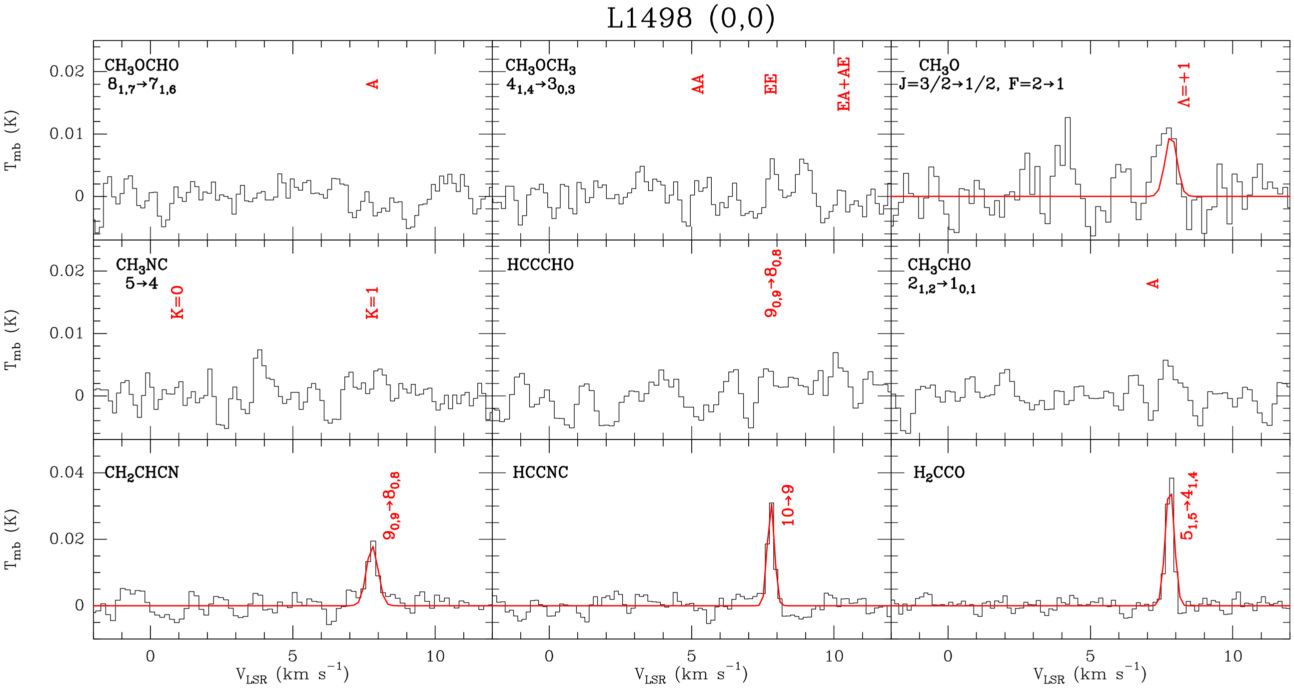

Figure 2. Sample of COM lines observed toward L1498's dust continuum peak. Red lines show the Gaussian line fits derived for the COMs and COM precursor transitions.

precursors. For O-bearing species, we have targeted methanol (CH_3OH), methoxy (CH_3O), CCCO, ketene (H_2CCO), formic acid (t-HCOOH), acetaldehyde (CH_3CHO), methyl formate (CH_3OCHO), dimethylether (CH_3OCH_3), cyclopropenone (c-C_3H_2O), and propynal (HCCCHO). As N-bearing COMs and precursors, we have cyanoacetylene (HC_3N), isocyanoacetylene (HCCNC), vinyl cyanide (CH_2CHCN) and methyl isocyanide (CH_3NC). A sample of their observed transitions is presented in Figures 2 and 3 for the dust and methanol peaks of the L1498 starless core, respectively.

Figures 2 and 3 show that species such as CH_3OH, CH_3O, CCCO, H_2CCO, HC_3N, HCCNC and CH_2CHCN, are detected either toward the dust or methanol peaks of the core, or toward both positions. The detected lines lie above the 3σ level in integrated intensity, where 1σ is calculated as $rms \times \sqrt{\Delta v \times \delta v}$, with rms and δv being respectively the noise level and velocity resolution of the spectra (Table 1), and Δv the linewidth of the line. We are confident about the detection of the lines because they all show central radial velocities $\sim$7.8 km s^{-1}, the V_{LSR} of the source. In addition, except for CCCO, we have covered at least two transitions for each detected species, which is enough for the correct identification of the molecular species since the level of line blending in starless/pre-stellar cores is expected to be low (linewidths of $\sim$0.3-0.4 km s^{-1}; see Table 2).

From Figures 2 and 3, and from Table 2, we find that the emission of the detected COMs and precursors tends to be brighter toward the position of the methanol peak with respect to the core's center except for CH_3O, which is only detected toward L1498's dust peak. Note, however, that the detected lines of CH_3O are weak (S/N=3.6; Table 2). For the rest of molecules (t-HCOOH, CH_3CHO, CH_3OCHO, CH_3OCH_3, c-C_3H_2O, HCCCHO, and CH_3NC), we have not detected any feature. The upper limits have been obtained from those transitions expected to be the brightest at the T_{ex} of the COM emission in the L1498 core (Section 3.2).

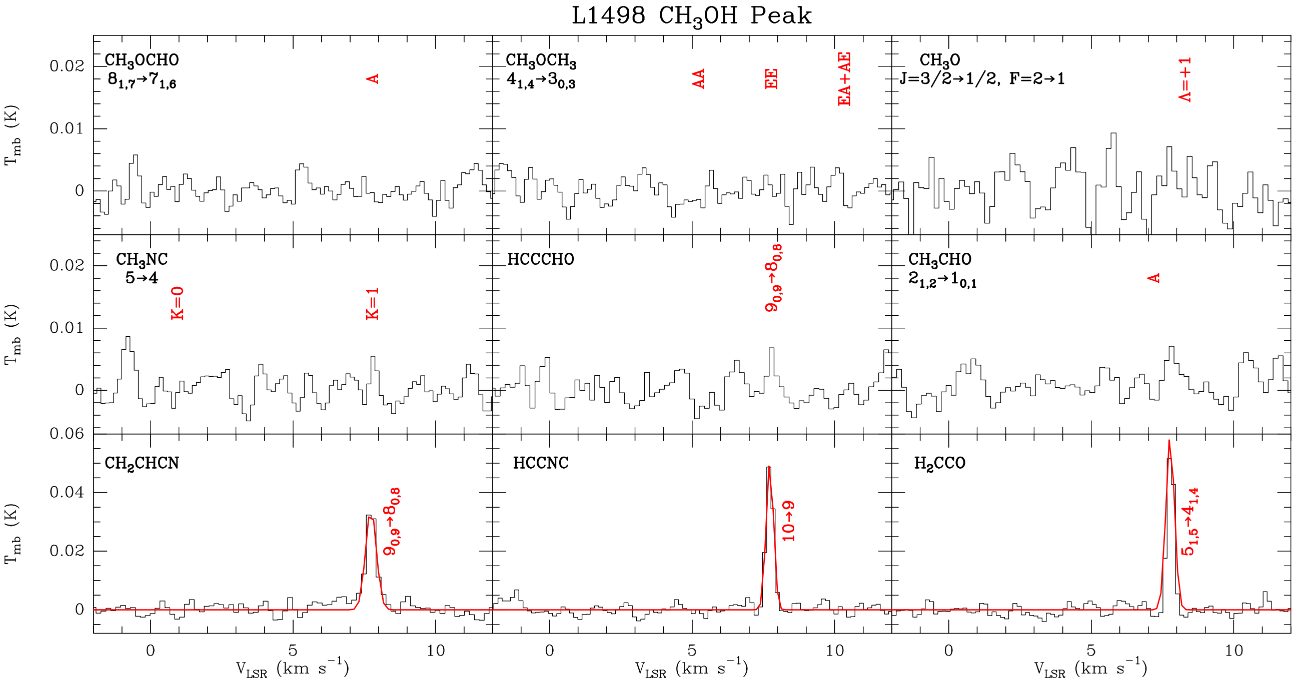

Figure 3. Sample of COM lines observed toward the position of the methanol peak in L1498. Red lines show the Gaussian line fits derived for the COMs and COM precursor transitions.

3.2. *Excitation analysis of COMs and COM precursors*

Except for CH_3OH (see below), the excitation temperature, T_{ex}, of the COM species with at least two transitions covered in our observations (i.e. H_2CCO, CH_2CHCN, HC_3N and HCCNC; see Table 2), has been determined using the SLIM package within MADCUBA. For CH_3O, the AUTOFIT tool did not converge because the targeted lines have similar upper level energies and therefore, the T_{ex} was fixed to that obtained for H_2CCO, another COM precursor (T_{ex}=5.8±0.8 K; Table 3). The same was done for CCCO, for which only one transition is available in our dataset. The T_{ex} derived from the COM emission lie between 4.1 and 6.4 K for the dust peak, and between 4.9 and 6.5 K toward the methanol peak. These T_{ex} are similar to those measured toward other starless/pre-stellar cores (see Vastel et al. 2014; Bizzocchi et al. 2014; Jiménez-Serra et al. 2016; Punanova et al. 2018; Harju et al. 2019; Scibelli & Shirley 2020), and suggest subthermal excitation of the COM emission in the L1498 core given that the kinetic temperature of the gas is ∼10 K within the inner ∼80" (or 11000 au; Tafalla et al. 2004).

The column densities of these COMs and COM precursors toward both the dust and methanol peaks in L1498 are reported in Table 3. The upper limits to the column densities of the molecular species not detected (e.g. CH_3OCHO or CH_3OCH_3) were calculated assuming T_{ex}=5.8 K and are also reported in this Table.

Table 2. COMs and COM precursors transitions covered in our L1498 observations and their derived line parameters

Species	Line	Frequency	**Dust peak**				**CH$_3$OH peak**			
			Area^b	Δv	V$_{\rm LSR}$	S/N^c	Area^b	Δv	V$_{\rm LSR}$	S/N^c
		(MHz)	(mK km s^{-1})	(km s^{-1})	(km s^{-1})		(mK km s^{-1})	(km s^{-1})	(km s^{-1})	
CH$_3$OH	$2_{0,2}\rightarrow1_{0,1}$ A	96741.371	140.0(1.5)^e	0.228(0.007)	7.796(0.004)	93.3	160.0(1.8)^e	0.224(0.004)	7.754(0.002)	88.9
	$2_{1,2}\rightarrow1_{1,1}$ A	95914.310	$\leq$4.5	...	...	...	$\leq$5.4	...	...	...
	$2_{1,1}\rightarrow1_{1,0}$ A	97582.798	$\leq$4.5	...	...	...	$\leq$5.4	...	...	...
	$2_{1,2}\rightarrow1_{1,1}$ E	96739.358	101.6(1.5)	0.22(0.01)	7.805(0.005)	23.4	116.3(1.8)	0.231(0.014)	7.753(0.006)	64.6
	$2_{0,2}\rightarrow1_{0,1}$ E	96744.545	18.9(1.5)	0.22(0.01)	7.805(0.005)	12.6	22.9(1.8)	0.231(0.014)	7.753(0.006)	12.7
	$2_{1,1}\rightarrow1_{1,0}$ E	96755.501	$\leq$4.5	...	...	...	$\leq$5.4	...	...	...
CH$_3$O^a	F=1$\rightarrow$0, Λ=-1	82455.98	$\leq$3.6	...	...	...	$\leq$2.4	...	...	...
	F=2$\rightarrow$1, Λ=-1	82458.25	4.3(1.2)^c	0.42(0.13)	7.84(0.06)	3.6	$\leq$2.4	...	...	...
	F=2$\rightarrow$1, Λ=+1	82471.82	4.3(1.2)	0.42(0.13)	7.84(0.06)	3.6	$\leq$2.4	...	...	...
	F=1$\rightarrow$0, Λ=+1	82524.18	$\leq$3.6	...	...	...	$\leq$2.4	...	...	...
CCCO	10$\rightarrow$9	96214.619	4.7(1.4)	0.3(0.1)	7.82(0.06)	3.4	16.0(1.8)	0.43(0.08)	7.82(0.03)	8.9
t-HCOOH	$1_{1,1}\rightarrow0_{0,0}$	87926.877	$\leq$1.5	...	...	...	$\leq$1.2	...	...	...
H$_2$CCO	$4_{1,3}\rightarrow3_{1,2}$	81586.230	19.2(1.2)	0.37(0.03)	7.79(0.01)	16	29.3(0.8)	0.35(0.03)	7.769(0.011)	36.6
	$5_{1,5}\rightarrow4_{1,4}$	100094.514	14.3(0.6)	0.37(0.03)	7.79(0.01)	23.8	22.3(0.8)	0.35(0.03)	7.769(0.011)	27.9
CH$_3$OCHO	$7_{2,6}\rightarrow6_{2,5}$ A	84454.754	$\leq$1.8	...	...	...	$\leq$1.5	...	...	...
CH$_3$OCH$_3$	$3_{1,3}\rightarrow2_{0,2}$ EE	82650.325	$\leq$3.6	...	...	...	$\leq$2.4	...	...	...
CH$_3$CHO	$5_{0,5}\rightarrow4_{0,4}$ A	95963.465	$\leq$5.3	...	...	...	$\leq$5.4	...	...	...
c-C$_3$H$_2$O	$6_{1,6}\rightarrow5_{1,5}$	79483.520	$\leq$4.2	...	...	...	$\leq$2.7	...	...	...
HCCCHO	$9_{0,9}\rightarrow8_{0,8}$	83775.842	$\leq$1.8	...	...	...	$\leq$1.5	...	...	...
CH3CN	$6_0\rightarrow5_0$	110383.500	$\leq$9.7	...	...	...	25.7(3.1)	0.32(0.05)	7.72(0.02)	8.3
	$6_1\rightarrow5_1$	110381.372	$\leq$9.7	...	...	...	17.2(3.1)	0.32(0.05)	7.72(0.02)	5.5
	$6_2\rightarrow5_2$	110374.989	$\leq$9.7	...	...	...	$\leq$9.3	...	...	...
CH$_3$NC	$5_0\rightarrow4_0$	100526.541	$\leq$1.7	...	...	...	$\leq$1.2	...	...	...
CH$_2$CHCN	$9_{0,9}\rightarrow8_{0,8}$	84946.000	6.3(0.6)	0.36(0.14)	7.78(0.06)	10.5	13.0(1.5)	0.34(0.08)	7.74(0.03)	8.7
	$9_{1,9}\rightarrow8_{1,8}$	83207.505	4.4(1.2)	0.36(0.14)	7.78(0.06)	3.7	8.9(1.5)	0.34(0.08)	7.74(0.03)	5.9
	$9_{1,8}\rightarrow8_{1,7}$	87312.812	3.8(0.5)	0.36(0.14)	7.78(0.06)	7.6	7.7(1.2)	0.34(0.08)	7.74(0.03)	6.4
	$10_{0,10}\rightarrow9_{0,9}$	94276.636	$\leq$3.9	...	...	...	6.6(0.8)	0.34(0.08)	7.74(0.03)	8.3
	$10_{1,9}\rightarrow9_{1,8}$	96982.442	$\leq$5.7	...	...	...	$\leq$5.4	...	...	...
HC$_3$N	9$\rightarrow$8	81881.468	856.7(1.2)	0.311(0.009)	7.794(0.003)	713.9	1102.2(0.8)	0.298(0.002)	7.718(0.001)	1377.8

Table 2 *continued*

Table 2 *(continued)*

Species	Line	Frequency	**Dust peak**				**CH_3OH peak**			
			Area^b	Δv	V_{LSR}	S/N^c	Area^b	Δv	V_{LSR}	S/N^c
		(MHz)	(mK km s^{-1})	(km s^{-1})	(km s^{-1})		(mK km s^{-1})	(km s^{-1})	(km s^{-1})	
	11→10	100076.392	380.6(0.6)	0.311(0.009)	7.794(0.003)	634.3	514.9(0.8)	0.298(0.002)	7.718(0.001)	643.6
HCCNC	8→7^d	79484.131	33.9(1.4)	0.42(0.05)	7.81(0.02)	24.2	49.1(2.7)	0.36(0.06)	7.742(0.024)	18.2
	10→9^d	99354.250	11.0(0.6)	0.42(0.05)	7.81(0.02)	18.3	17.7(0.4)	0.36(0.06)	7.742(0.024)	44.3

NOTE—Line profiles were fitted using MADCUBA (see Section 3.2).$^{(a)}$ Hyperfine components of the N=1-0, K=0, J=3/2→1/2 transition of CH_3O. $^{(b)}$ Upper limits are calculated as $3\times rms\times\sqrt{\Delta v \times \delta v}$, with rms the noise level, Δv the linewidth and δv the velocity resolution of the spectrum. $^{(c)}$ This refers to the S/N ratio in integrated intensity area. $^{(d)}$ Hyperfine structure not resolved. $^{(e)}$ Errors in the line area are calculated as $rms\times\sqrt{\Delta v \times \delta v}$.

For CH_3OH (A and E species), we used RADEX instead of MADCUBA (van der Tak et al. 2007) because MADCUBA performs the fitting of the molecular lines using the LTE approximation. We assume a kinetic temperature of T_{kin}=10 K (Tafalla et al. 2004). The fit of the CH_3OH lines was achieved considering an H_2 gas density of $\sim4\times10^4\,cm^{-3}$ (consistent with the one expected from the H_2 radial gas density profile derived by Tafalla et al. (2004) at a distance of ∼83"; see Section 5) and assuming column densities of $3.1\times10^{12}\,cm^{-2}/3.4\times10^{12}\,cm^{-2}$ for the A/E species toward L1498's dust peak, and of $4.7\times10^{12}\,cm^{-2}/4.0\times10^{12}\,cm^{-2}$ for the A/E species toward the methanol peak. The CH_3OH A/E abundance ratios are ∼0.9 and ∼1.2 toward the dust and methanol peaks, respectively. These values are similar to those derived toward L1544 and other molecular dark clouds such as L183, TMC-1 or B335 (Friberg et al. 1988; Bizzocchi et al. 2014), and fall between the expected high temperature value of ∼1.0 and the one at 10 K (∼0.7; see Wirström et al. 2011).

3.3. *COM abundance profiles in L1498*

To calculate the abundances of the observed COMs and precursors, we need to determine the H_2 column density toward the dust and methanol peaks of L1498. For the core center, we use the H_2 column density of $\sim3.5\times10^{22}\,cm^{-2}$ inferred by Tafalla et al. (2004) from MAMBO 1.2 mm data. The H_2 gas density profile of the L1498 starless core is flat within the inner 30", which engulfs the radius associated with half the beam of the IRAM 30 m observations at 3 mm (radius of ∼13"). For the position of the methanol peak, we use the H_2 column density map of the Taurus molecular cloud obtained by Spezzano et al. (2016) from *Herschel* data at 250, 350 and 500 μm assuming a dust optical depth index of β=1.5. The H_2 column density toward L1498's methanol peak (i.e. at a distance of ∼83" with respect to the core's center) is $7.2\times10^{21}\,cm^{-2}$. While the H_2 column density of $\sim3.5\times10^{22}\,cm^{-2}$ toward the dust peak corresponds to a visual extinction of $A_v\sim37$ mag, the H_2 column density of $7.2\times10^{21}\,cm^{-2}$ measured toward the methanol peak corresponds to a visual extinction of $A_v\sim7.7$ mag using the Bohlin et al. (1978) formula (or $N(H_2/A_v)=0.94\times10^{21}\,cm^{-2}$).

Table 3 reports the derived abundances of the COMs and COM precursors shown in Table 2. Table 3 reveals a general trend for these species to be enhanced toward the position of the methanol peak of L1498. The O-bearing species present the largest enhancements with CCCO and H_2CCO being, respectively, factors of ∼14 and ∼8 more abundant toward the methanol peak than toward the core center. For the N-bearing molecules, their abundances are enhanced by factors ∼4-6 toward the outer part of the L1498 starless core. This COM enhancement is similar to that reported toward the L1544 pre-stellar core (Jiménez-Serra et al. 2016). In Section 4, we compare the COM and COM precursor abundance profiles measured toward these two cores, L1498 and L1544.

We note that the H_2 column density derived for the position of the dust peak but using *Herschel* data is $\sim10^{22}\,cm^{-2}$, a factor of ∼4 lower than that measured by MAMBO at 1.2 mm. This is due to the fact that *Herschel* underestimates the total amount of dust present toward this region because it preferentially probes the dust grain population from the outer layers of the core (Chacón-Tanarro et al. 2019) and the large beam can dilute possible centrally concentrated structures, as toward the center of L1544. This is the reason why we use the millimeter data for measuring the total H_2 column density toward the innermost regions of L1498.

For the position of the methanol peak, the H_2 column density measured using *Herschel* and MAMBO data are similar. Indeed, the

Table 3. Excitation temperatures, column densities, and abundances of COMs and COM precursors toward the dust and methanol peaks in L1498

Molecule	**Dust Peak**			**Methanol Peak**		
	T_{ex}	N_{obs} (cm^{-2})	$\chi_{obs}{}^{a}$	T_{ex}	N_{obs} (cm^{-2})	$\chi_{obs}{}^{a}$
CH_3OH-A	10^{d}	$3.1\times10^{12\,d}$	$8.9\times10^{-11\,d}$	10^{d}	$4.7\times10^{12\,d}$	$6.5\times10^{-10\,d}$
CH_3OH-E	10^{d}	$3.4\times10^{12\,d}$	$9.7\times10^{-11\,d}$	10^{d}	$4.0\times10^{12\,d}$	$5.6\times10^{-10\,d}$
CH_3OH (Total)	...	$6.5\times10^{12\,d}$	$1.9\times10^{-10\,d}$	...	$8.7\times10^{12\,d}$	$1.2\times10^{-9\,d}$
CH_3O	5.8^{b}	$(1.2\pm0.4)\times10^{11}$	$(3.6\pm1.2)\times10^{-12}$	6.0^{b}	$\leq1.2\times10^{11}$	$\leq1.7\times10^{-11}$
CCCO	5.8^{b}	$(3.9\pm1.5)\times10^{11}$	$(1.2\pm0.5)\times10^{-11}$	6.0^{b}	$(1.2\pm0.2)\times10^{12}$	$(1.7\pm0.3)\times10^{-10}$
t-HCOOH	5.8^{b}	$\leq4.6\times10^{12}$	$\leq1.4\times10^{-10}$	6.0^{b}	$\leq6.6\times10^{12}$	$\leq9.2\times10^{-10}$
H_2CCO	5.8 ± 0.8^{c}	$(2.6\pm0.6)\times10^{12}$	$(7.8\pm1.8)\times10^{-11}$	6.0 ± 0.3^{c}	$(4.5\pm0.2)\times10^{12}$	$(6.2\pm0.3)\times10^{-10}$
CH_3OCHO	5.8^{b}	$\leq1.3\times10^{12}$	$\leq3.9\times10^{-11}$	6.0^{b}	$\leq1.1\times10^{12}$	$\leq1.5\times10^{-10}$
CH_3OCH_3	5.8^{b}	$\leq3.9\times10^{11}$	$\leq1.2\times10^{-11}$	6.0^{b}	$\leq4.4\times10^{11}$	$\leq6.1\times10^{-11}$
CH_3CHO	5.8^{b}	$\leq3.0\times10^{11}$	$\leq9.0\times10^{-12}$	6.0^{b}	$\leq1.4\times10^{11}$	$\leq1.9\times10^{-11}$
c-C_3H_2O	5.8^{b}	$\leq3.9\times10^{10}$	$\leq1.2\times10^{-12}$	6.0^{b}	$\leq2.9\times10^{10}$	$\leq4.0\times10^{-12}$
HCCCHO	5.8^{b}	$\leq2.0\times10^{11}$	$\leq6.0\times10^{-12}$	6.0^{b}	$\leq2.0\times10^{11}$	$\leq2.8\times10^{-11}$
CH_3CN	5.6^{b}	$\leq8.3\times10^{10}$	$\leq2.4\times10^{-12}$	15.9 ± 5.8	$(1.0\pm0.1)\times10^{11}$	$(1.4\pm0.1)\times10^{-11}$
CH_3NC	5.6^{b}	$\leq1.0\times10^{10}$	$\leq3.0\times10^{-13}$	6.0^{b}	$\leq7.8\times10^{9}$	$\leq1.1\times10^{-12}$
CH_2CHCN	4.1 ± 0.3^{c}	$(1.3\pm0.4)\times10^{12}$	$(3.9\pm1.2)\times10^{-11}$	4.9 ± 0.3^{c}	$(1.1\pm0.2)\times10^{12}$	$(1.5\pm0.3)\times10^{-10}$
HC_3N	6.4 ± 0.3^{c}	$(1.6\pm0.3)\times10^{13}$	$(4.8\pm0.9)\times10^{-10}$	6.5 ± 0.7^{c}	$(2.2\pm1.0)\times10^{13}$	$(3.1\pm1.4)\times10^{-9}$
HCCNC	5.6 ± 0.9^{c}	$(7.8\pm4.0)\times10^{11}$	$(2.4\pm1.2)\times10^{-11}$	6.0 ± 1.3^{c}	$(9.4\pm5.7)\times10^{11}$	$(1.3\pm0.8)\times10^{-10}$

NOTE—$^{(a)}$ Molecular abundances calculated using an H_2 column density of 3.5×10^{22} cm^{-2} for the dust continuum peak and of 7.2×10^{21} cm^{-2} for the position of the methanol peak (see Section 3.3 for details). $^{(b)}$ Fitting solutions could only be obtained by fixing T_{ex} within the MADCUBA-SLIM tool (Martín et al. 2019). $^{(c)}$ Errors correspond to 1σ uncertainties in MADCUBA. ^{d} The CH_3OH column densities have been calculated using RADEX (van der Tak et al. 2007). The value under T_{ex} refers to the assumed kinetic temperature T_{kin} in the RADEX calculations.

Table 4. Excitation temperatures, column densities, and abundances of CH_3OH, CCCO, H_2CCO, t-HCOOH and HC_3N toward the dust and methanol peaks in L1544

Molecule	**Dust Peak**			**Methanol Peak**		
	T_{ex}	N_{obs} (cm^{-2})	$\chi_{obs}{}^{a}$	T_{ex}	N_{obs} (cm^{-2})	$\chi_{obs}{}^{a}$
CH_3OH-A	...	$0.7\times10^{13\ d}$	$0.2\times10^{-9\ d}$	...	$2.4\times10^{13\ d}$	$4\times10^{-9\ d}$
CH_3OH-E	...	$0.7\times10^{13\ d}$	$0.2\times10^{-9\ d}$	...	$2.4\times10^{13\ d}$	$4\times10^{-9\ d}$
CH_3OH (Total)	...	$1.4\times10^{13\ d}$	$0.4\times10^{-9\ d}$	...	$4.8\times10^{13\ d}$	$8\times10^{-9\ d}$
CCCO	5.6 ± 1.3^{c}	$(8.9\pm1.2)\times10^{11\ e}$	$(1.7\pm0.2)\times10^{-11}$	5.9^{b}	$(7.2\pm1.3)\times10^{11\ e}$	$(4.8\pm0.9)\times10^{-11}$
t-HCOOH	12.6 ± 6.9^{c}	$(4.8\pm0.9)\times10^{11\ e}$	$(8.9\pm1.7)\times10^{-12}$	5.9^{b}	$(4.0\pm1.2)\times10^{10\ e}$	$(2.7\pm0.8)\times10^{-12}$
H_2CCO	$4.9\pm0.2^{\ f}$	$(1.5\pm0.2)\times10^{13\ f}$	$(2.8\pm0.4)\times10^{-10}$	5.9 ± 0.8^{c}	$(9.8\pm2.3)\times10^{12\ e}$	$(6.5\pm1.5)\times10^{-10}$
CH_3CN	8.7 ± 1.3^{c}	$(1.5\pm0.2)\times10^{11\ e}$	$(2.8\pm0.4)\times10^{-12}$	5.9^{b}	$\leq9.1\times10^{10\ e}$	$\leq6.1\times10^{-12}$
HC_3N	5.5 ± 0.2^{c}	$(1.0\pm0.3)\times10^{14\ e}$	$(1.9\pm0.6)\times10^{-9}$	4.8^{b}	$(4.2\pm0.4)\times10^{13\ e}$	$(2.8\pm0.3)\times10^{-9}$

NOTE—$^{(a)}$ Molecular abundances calculated using an H_2 column density of 5.4×10^{22} cm^{-2} for the dust continuum peak and of 1.5×10^{22} cm^{-2} for the position of the methanol peak (Jiménez-Serra et al. 2016). $^{(b)}$ Fitting solutions could only be obtained by fixing T_{ex} within the MADCUBA-SLIM analysis tool (Martín et al. 2019). $^{(c)}$ Errors correspond to 1σ uncertainties in MADCUBA. $^{(d)}$ Taken from the non-LTE analysis carried out by Punanova et al. (2018). $^{(e)}$ Obtained using the data from Jiménez-Serra et al. (2016). $^{(f)}$ Note that this molecule was also observed by Vastel et al. (2014) but they obtained a T_{ex}=27±1 K. We thus use the data from Jiménez-Serra et al. (2016), which give a closer T_{ex} to the ones inferred for the other species.

H_2 column density obtained from the MAMBO 1.2 mm map is $\sim1.3\times10^{22}\,cm^{-2}$, i.e. only a factor ~1.8 higher than that derived using *Herschel* ($7.2\times10^{21}\,cm^{-2}$; see above). This factor is smaller than the COMs abundance enhancements measured in L1498's methanol peak with respect to the core center (~4-14), which implies that the observed increase in the abundance of COMs toward the outer regions of L1498 is real. We opt for the use of the *Herschel*-based H_2 column density toward L1498's methanol peak, because: i) the calculation and comparison with the COMs abundances toward L1544 is done in the same manner (see Jiménez-Serra et al. 2016); ii) the *Herschel* beam of ~35" is closer to the one of the IRAM 30 m observations (~30" vs. ~11" of the MAMBO observations); and iii) the MAMBO observations toward the outer parts of the core may be affected by large-scale filtering produced by the chopping technique used in ground-based telescopes.

4. COMPARISON WITH L1544

Vastel et al. (2014) reported the abundances of the COMs and precursor species CH_3OH, CCCO, H_2CCO and t-HCOOH toward the dust peak of the L1544 pre-stellar core. In Jiménez-Serra et al. (2016), two different positions in this core were observed but no abundances were provided for the latter COM precursor species. Therefore, in this Section, we take the abundances of CH_3OH (A and E species) from Punanova et al. (2018, who obtained a radial profile of the abundance of CH_3OH), and calculate the abundances of CCCO, H_2CCO and t-HCOOH toward both the dust and methanol peaks of L1544 using the IRAM 30 m data from Jiménez-Serra et al. (2016, please refer to this article for the details on the observations). In this way, we can compare these results with those obtained toward the L1498 starless core. In our analysis, we also include the N-bearing molecules HC_3N and CH_3CN.

Table 4 collects the excitation temperatures (T_{ex}), column densities (N_{obs}), and molecular abundances of all these molecules measured toward the dust and methanol peaks of L1544. Note that the column densities derived for these species toward the dust peak of L1544 are very similar to those calculated independently by Lattanzi et al. (2020) for the same position within this core.

In Figure 4, we present the comparison of the abundances of COMs and COM precursors measured toward the dust peaks and methanol peaks of the cold cores L1544 (yellow and red, respectively) and L1498 (cyan and dark blue, respectively). As mentioned in Section 3.3, all the detected COMs and COM precursors, except t-HCOOH in L1544, are enhanced toward the position of the methanol peaks in both L1498 and L1544. However, the abundances of O-bearing and N-bearing species are significantly different in L1498 with respect to L1544. While large O-bearing COMs such as CH_3CHO, CH_3OCHO or CH_3OCH_3 are clearly detected in L1544, we only report upper limits to the abundance of these molecules in L1498. Especially clear is the case of CH_3CHO, which is relatively abundant in L1544 (with an abundance of $\sim2\times10^{-10}$ toward the methanol peak; Figure 4), but it is not detected in L1498. Interestingly, the COM precursor CH_3O shows an opposite behaviour toward both cores: while CH_3O is clearly enhanced toward the methanol peak of L1544, this molecule is only detected toward the core center of L1498. However, note that the upper limit to the abundance of CH_3O toward L1498's methanol peak is still consistent with a possible enhancement of this species in the outer shells of the core.

For the N-bearing COMs and precursors, Figure 4 shows that these species not only are in general more abundant toward L1498 than

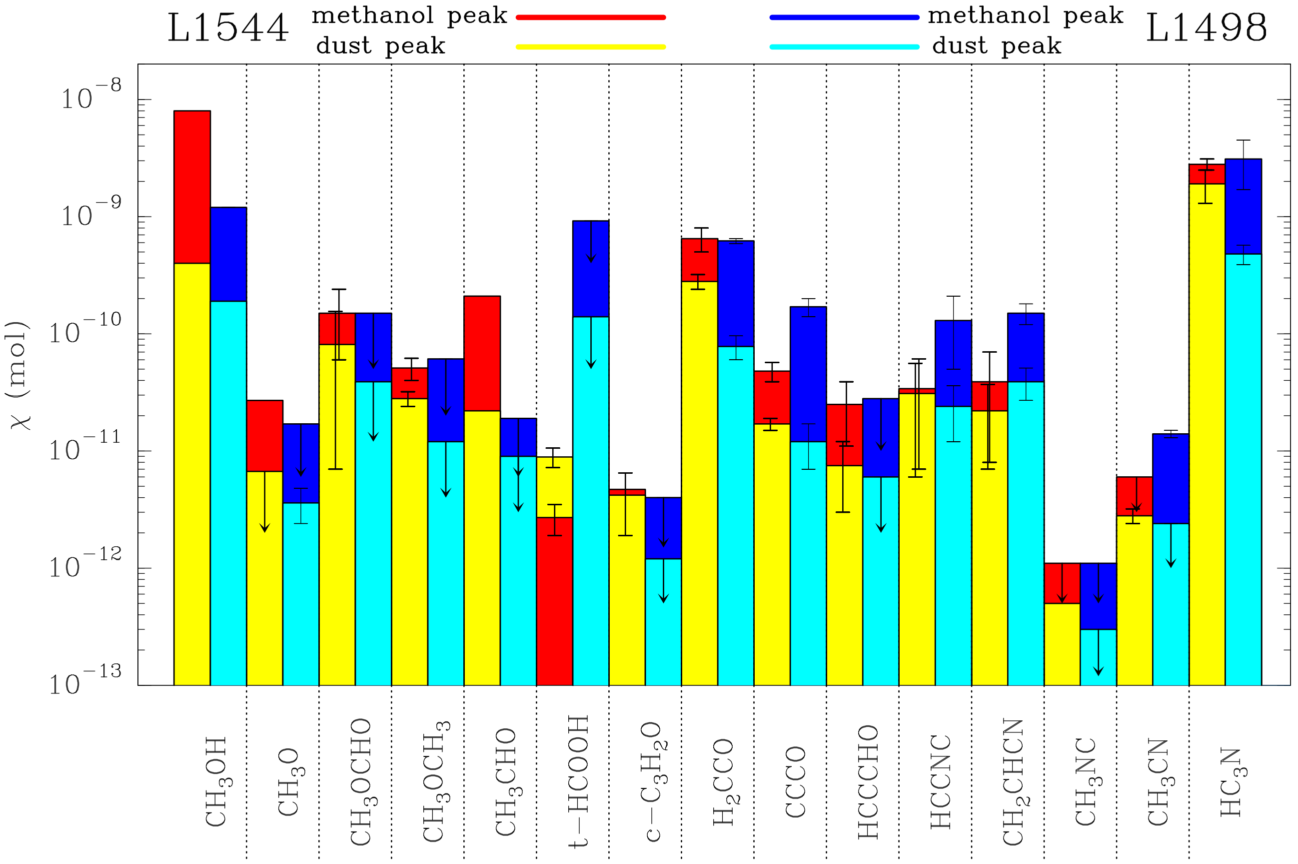

Figure 4. Histogram comparing the abundances of COMs and COM precursors measured toward the methanol and dust peaks in L1498 and L1544. Molecules are labeled at the bottom. Error bars correspond to 1σ uncertainties in the column densities calculated by MADCUBA, and arrows indicate upper limits. Color legend is as follows: red - methanol peak in L1544; yellow - dust peak in L1544; dark blue - methanol peak in L1498; and cyan - dust peak in L1498. The abundances of the COMs and COM precursors have either been extracted from Jiménez-Serra et al. (2016) and Punanova et al. (2018), or have been calculated from the data used in Jiménez-Serra et al. (2016).

in L1544, but they also present larger enhancements toward L1498's methanol peak than toward the one in L1544 (the enhancements are by factors 4-6 in L1498 vs. factors 1.2-1.8 in L1544; see Section 3.3 and Jiménez-Serra et al. 2016). As discussed in Section 5, the observed differences in the abundance profiles of O-bearing and N-bearing species in L1498 and L1544 are due to the different physical structure of the cores, which in turn is likely associated with their evolutionary stage.

5. MODELLING THE FORMATION OF COMS IN L1498

To understand the observed abundances of O-bearing and N-bearing COMs in L1498 and their differences with respect to L1544, we have modelled the chemistry of COMs using the 1D approach previously used in Vasyunin et al. (2017) but applied to the case of L1498. The 1D density profile of the L1498 core was taken from Tafalla et al. (2004, see their Table 2) and is:

$$n(r) = \frac{0.94 \times 10^5}{1 + (r('')/75'')^{3.5}} \text{ cm}^{-3}. \qquad (1)$$

As temperature radial profile, we have used the T$_{kin}$ values derived by Tafalla et al. (2004) from NH_3 observations for L1498 (see their

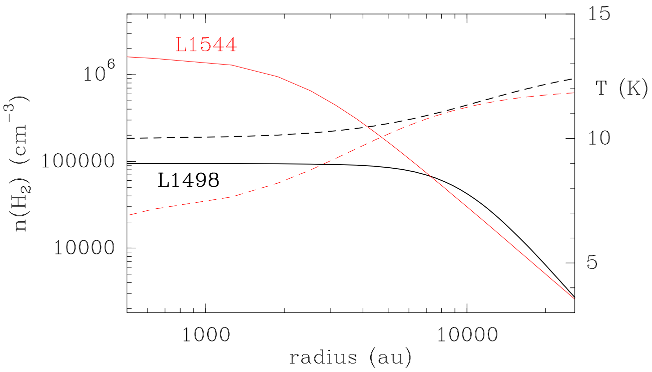

Figure 5. Radial distribution of the H_2 volume gas density (solid lines) and temperature (dashed lines) assumed for the L1498 starless core as a function of radius (in black; see also Section 5 and Tafalla et al. 2004). For comparison, we also show the physical structure of the L1544 pre-stellar core determined by Chacón-Tanarro et al. (2019, in red).

Section 3.1 and Figure 4) and assumed a temperature radial distribution similar to the one employed by Chacón-Tanarro et al. (2019) for the L1544 pre-stellar core. We also assume that the gas and dust temperatures are equal. The temperature profile is fitted as:

$$T(r) = 13.0 - \frac{13.0 - 10.0}{1.0 + (r('')/90'')^{1.7}}\ \mathrm{K}. \qquad (2)$$

The radial distribution of the H_2 volume gas density and temperature assumed for the L1498 starless core are shown in Figure 5 (see also Tafalla et al. 2004). For comparison, in this Figure we have also included the physical structure derived by Chacón-Tanarro et al. (2019) for the L1544 pre-stellar core. From Figure 5, it is clear that the physical structure of both cores is different: L1498 shows a flatter gas density profile and lower peak H_2 gas density with respect to L1544, and its temperature at the center never gets below 10 K as observed in L1544.

Using the physical structure of L1498, the chemical evolution of the core is then calculated toward 150 radial points with 1" spatial spacing. To simulate the chemical evolution at every radial point, we utilized the 0D gas-grain chemical model MONACO. This is a rate equations-based, three-phase (gas/ice surface/ice bulk) numerical model that provides the evolution of the fractional abundances of atomic and molecular species with time. The model is based on the work by Vasyunin & Herbst (2013) and was successfully applied to reproduce the abundances of O-bearing COMs in the prototypical L1544 pre-stellar core (Vasyunin et al. 2017). In this model, the precursors of both O-bearing and N-bearing COMs are formed on the surface of dust grains via hydrogenation. Once formed, a small fraction of these precursors is non-thermally desorbed from dust grains (see details below on the non-thermal processes assumed) and undergoes subsequent gas-phase reactions that produce the observed COMs (see Vasyunin & Herbst 2013; Vasyunin et al. 2017).

Before this study, minor updates had been introduced in the chemical network of the MONACO code as described in Lattanzi et al. (2020, see the reactions described in their Table 2). However, in our work, we have found an enhanced set of N-bearing species, which includes species such as CH_2CHCN, HCCNC and CH_3NC. Thus, we have further expanded our chemical network to account properly for the chemistry of those species. In particular, we have expanded the gas and grain chemistry of hydrocarbons (CxHy) following Hickson et al. (2016). This has enabled us to add the formation route of CH_2CHCN via the gas-phase reactions $N + C_3H_5 \rightarrow CH_2CHCN + H_2$ presented in the KIDA database, to the gas-phase and grain-surface routes already present in our network, namely the surface hydrogenation of HC_3N and the gas-phase reaction $CN + C_2H_4 \rightarrow CH_2CHCN + H$. We note, however, that the reaction between N and C_3H_5 has not been studied in detail, and it may not lead to CH_2CHCN as a product (J.-C. Loison; private communication). The chemical networks of HCCNC and CH_3NC were added following the approach described in Vastel et al. (2019) and Willis et al. (2020).

It has been shown before that interstellar chemistry is an interplay between gas-phase and grain-surface chemical processes connected via the processes of accretion and desorption, and with surface chemistry being especially important for the formation of COMs (see e.g. Herbst & van Dishoeck 2009; Agúndez & Wakelam 2013). At the low temperatures of 10 K typical of pre-stellar cores, desorption of species from dust grains to the gas phase requires additional energy which is either the result of exothermic surface reactions, or the result of the interaction of icy grain mantles with energetic particles such as cosmic rays or photons produced by cosmic rays. Although the details are still known poorly, many observational results such as widespread presence of methanol in cold gas imply non-zero efficiency of desorption from grains even at 10 K.

In our model, in addition to thermal evaporation, photodesorption, cosmic ray-induced desorption (Hasegawa et al. 1993) and reactive (chemical) desorption (Minissale et al. 2016) are included. While cosmic ray-induced desorption is known to have limited effects on the abundances of COMs, the case of reactive desorption is more complicated. Several theoretical and experimental studies of reactive desorption arrive to somewhat different conclusions on reactive desorption efficiency for various chemically reacting systems (see Garrod et al. 2007; Minissale et al. 2016; Chuang et al. 2018; Fredon & Cuppen 2018). The point of consensus is probably that the COMs with a large number of atoms (>6) do not desorb from grains via the mechanism of reactive desorption because the energy released during the exothermic surface reaction event likely gets redistributed and relaxed between the numerous internal degrees of freedom of a product molecule rather than breaking the bond between the product molecule and the surface. In this study, we use the parametrization of the efficiency of reactive desorption proposed in Minissale et al. (2016), the same as in Vasyunin et al. (2017). Note that a natural outcome of this parameterization is that the efficiency of chemical reactive desorption for large COMs (with more than 6 atoms such as e.g. CH_2CHCN) is negligible (see below).

Other assumptions made for the surface chemistry are also the same as in Vasyunin et al. (2017): the tunneling for surface diffusion of H and H_2 is enabled; and the diffusion-to-binding energy ratio E_{diff}/E_{bind}=0.3. The initial abundances of the species considered in the modeling were obtained from the final abundances of the simulation of a diffuse cloud model with A_V=2 mag, gas and dust temperatures of 20 K and gas density of 10^2 cm^{-3} over 10^7 years using the "low metals"' initial abundances EA1 from Wakelam & Herbst (2008).

Using the physical and chemical set-up described above, we performed the chemical modeling of the L1498 starless core over a time span of 10^6 years and compared the modeling results with our observations. We found that the best fit between the observed and the predicted fractional abundances of the O-bearing and N-bearing COMs (calculated using the modelled column densities convoluted with the 26" IRAM 30m beam) is reached at an age of 9×10^4 years for the L1498 starless core. The best-fit COMs abundances are presented in Table 5, where we consider that the observed and predicted abundances are in agreement if both differ by less than a factor of 10.

In Figure 6, we report the results of the abundance distribution of O-bearing and N-bearing COMs as a function of radius obtained for the L1498 starless core for our best-fit model. Interestingly, the predicted COMs abundances show a maximum in their distribution at a radial distance between 10000 au and 14000 au, which is consistent with the observed behaviour (Tafalla et al. 2006). Note that this distance is three times further away than found toward L1544 (∼4000 au in L1544; see Vasyunin et al. 2017) and it is a consequence of the flatter density distribution of the L1498 starless core. Our model also reproduces the lack of detections of O-bearing COMs such as CH_3OCHO and CH_3OCH_3 in L1498 as opposed to L1544. Indeed, the predicted abundances of these molecules for our L1498 model fall well below the value of 1×10^{-12}, which is consistent with the measured upper limits for these species toward this core (see Table 3 and Section 3).

Note, however, that the COM and COM precursor abundance enhancement predicted by the model at distances ∼11000 au, is less pronounced than that predicted by the same model for L1544. This is probably due to the fact that the H_2 gas density toward L1498's dust peak is moderate ($\sim10^5$ cm^{-3}, i.e. two orders of magnitude lower than that measured for L1544) and thus, it does not induce such a strong molecular depletion in the L1498's model compared to L1544's one. The angular resolution of the MAMBO 1.2 mm map of L1498 is however of ∼11" and, as in the case of L183 (Lattanzi et al. 2020), we cannot rule out the possibility that within the innermost ≤2000 au of L1498 the actual H_2 gas density is higher than $\sim10^5$ cm^{-3}, as derived by Tafalla et al. (2004).

Despite this caveat, Table 5 shows that our model matches (overall) the abundances of most O-bearing and N-bearing COMs and COM precursors measured toward L1498, with the exception of CH_3OH and CH_2CHCN[5]. For CH_3OH, our model overproduces this molecular species in the gas phase toward L1498's dust peak by a factor of ∼40 while it predicts an abundance within a factor of ∼7 for the position of the methanol peak. Note that this overproduction was already noted by Punanova et al. (2018) for the case of L1544, although in the case of L1498 it is more likely related to a milder depletion of the molecular gas toward the innermost regions of the core (see above).

For CH_2CHCN, this molecule is firmly detected toward both positions in the L1498 starless core with abundances of (1.3-1.6)$\times10^{-10}$ (Table 5), while the modelled values are up to three orders of magnitude lower. The low abundance of CH_2CHCN is maintained not only at the moment of the best agreement between the model and observations, but over the whole time span of the simulation: it never exceeds a few $\times10^{-12}$. This means that the proposed gas-phase formation routes of CH_2CHCN (i.e. $N + C_3H_5 \rightarrow CH_2CHCN + H_2$ and $CN + C_2H_4 \rightarrow CH_2CHCN + H$, see above) are not sufficient to produce the observed amount of this species in the L1498 starless core. Alternatively, on grain surfaces CH_2CHCN forms mainly via the hydrogenation of HC_3N. However, this grain surface formation does not contribute significantly to the gas phase abundance of CH_2CHCN due to the near-zero efficiency of reactive desorption of this species from the grains (of $\sim10^{-6}$, as calculated following the formalism of Minissale et al. 2016). This is in agreement with Garrod et al. (2017) who also arrived to the conclusion that the modelled gas-phase abundance of CH_2CHCN does not exceed 10^{-11} at low temperatures.

To reproduce the abundances of CH_2CHCN measured toward L1498, we have tested arbitrary values for the efficiency of reactive desorption of this species. An efficiency of 1% is sufficient to reproduce the observed gas phase abundance of 1.5×10^{-10} for CH_2CHCN simultaneously with the rest of species. This implies that either chemical reactive desorption is somehow efficient for this molecule in particular, or that there is an additional mechanism responsi-

---

[5] H_2CCO shows a disagreement by a factor of just ∼10 toward the position of L1498's methanol peak (Table 5).

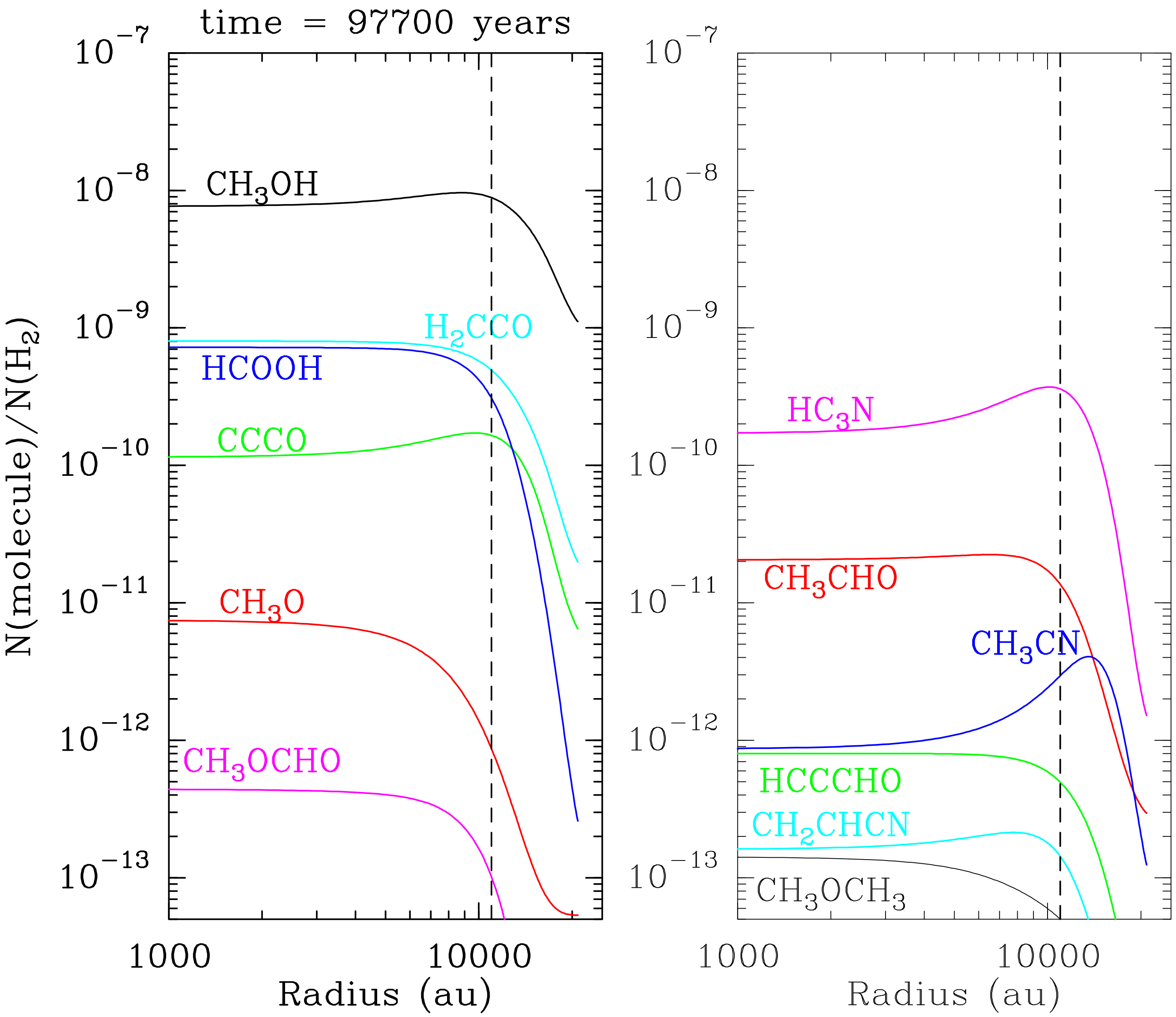

Figure 6. Radial distributions of modeled fractional abundances of species considered in this study. Fractional abundances are derived as column density ratios convolved with a 26” beam. A radius r=0 au corresponds to the location of the dust peak. Vertical dashed lines indicate the radius associated with the location of the methanol peak in L1498.

ble for the desorption of these large COMs besides chemical reactive desorption. The direct impact of cosmic rays on dust grains has been proposed to be a factor of 10 more efficient than chemical reactive desorption (see Dartois et al. 2019, 2020), which could increase the desorption efficiency of large COMs from grains. Note, however, that if this were the case, CH_2CHCN would have to survive on the grain surface over the period between its formation and independent desorption, which in our current model is unlikely because this molecule is further hydrogenated into ethyl cyanide (C_2H_5CN) on the grain surface. Further experimental and theoretical work on the grain chemistry and desorption mechanisms of N-bearing COMs such as C_2H_5CN at low temperatures is needed.

We finally note that the best-fit chemical age derived for L1498 is shorter than that for L1544 (9×10^4 years vs. 1.6×10^5 years; Vasyunin et al. 2017). L1498 indeed shows a flatter density profile distribution than L1544 and its deuterium fractionation is consistent with the core being at an earlier evolutionary stage (Tafalla et al.

Table 5. Measured and modelled abundances of complex organic molecules in L1498

	Dust peak			Methanol peak		
Species	$N(X)/N(H_2)_{obs}$	$N(X)/N(H_2)_{mod}$	Agreement	$N(X)/N(H_2)_{obs}$	$N(X)/N(H_2)_{mod}$	Agreement
CH_3OH	1.9×10^{-10}	7.7×10^{-9}	$-$	1.2×10^{-9}	8.6×10^{-9}	$+$
CH_3O	3.6×10^{-12}	7.5×10^{-12}	$+$	$\leq1.7\times10^{-11}$	7.3×10^{-13}	$+$
C_3O	1.2×10^{-11}	1.1×10^{-10}	$+$	1.7×10^{-10}	1.6×10^{-10}	$+$
HCOOH	$\leq1.4\times10^{-10}$	7.2×10^{-10}	$+$	$\leq9.2\times10^{-10}$	2.7×10^{-10}	$+$
H_2CCO	7.8×10^{-11}	8.0×10^{-10}	$-$	6.2×10^{-10}	4.6×10^{-10}	$+$
$HCOOCH_3$	$\leq3.9\times10^{-11}$	4.4×10^{-13}	$+$	$\leq1.5\times10^{-10}$	8.3×10^{-14}	$+$
CH_3OCH_3	$\leq1.2\times10^{-11}$	1.4×10^{-13}	$+$	$\leq6.1\times10^{-11}$	4.7×10^{-14}	$+$
CH_3CHO	$\leq9.0\times10^{-12}$	2.1×10^{-11}	$+$	$\leq1.9\times10^{-11}$	1.2×10^{-11}	$+$
HCCCHO	$\leq7.2\times10^{-12}$	8.0×10^{-13}	$+$	$\leq3.2\times10^{-11}$	4.6×10^{-13}	$+$
CH_3CN	$\leq2.4\times10^{-12}$	8.7×10^{-13}	$+$	1.4×10^{-11}	3.0×10^{-12}	$+$
CH_3NC	$\leq3.0\times10^{-13}$	8.7×10^{-13}	$+$	$\leq1.1\times10^{-12}$	3.2×10^{-12}	$+$
CH_2CHCN	3.9×10^{-11}	1.6×10^{-13}	$-$	$1.5e\times10^{-10}$	1.3×10^{-13}	$-$
HC_3N	5.0×10^{-10}	1.7×10^{-10}	$+$	3.2×10^{-9}	3.5×10^{-10}	$+$

2004; Crapsi et al. 2005). The younger chemical age of L1498 is also supported by the smaller abundance difference found for methanol between its dust and methanol peaks, with respect to that measured toward L1544 (see Figure 4). This can be explained by the smaller degree of CO freeze-out in L1498, which in turn indicates a less evolved core for L1498 as compared to L1544. A shorter age would also explain why L1498 is accreting material from the molecular cloud onto the core, but does not show any infall signatures within the core itself yet (Tafalla et al. 2004).

6. CONCLUSIONS

As shown in Section 3, our high-sensitivity observations carried out toward the L1498 starless core reveal that O-bearing COMs such as CH_3CHO, CH_3OCHO and CH_3OCH_3 are not detected neither toward the dust peak nor toward the outer regions of the core where CH_3OH peaks (i.e. at ∼10000 au from the core's center). This behaviour is in contrast with the one observed toward the L1544 pre-stellar core, where these large O-bearing COMs not only are detected toward this outer region, but their abundances present their maximum values at a distance of only ∼4000 au with respect to the center of the L1544 core.

For N-bearing COMs, these species are systematically enhanced toward the outer regions of the L1498 starless core in agreement with what was previously found toward L1544, and even in higher amounts. The distance at which the enhancement of the N-bearing COMs occurs in L1498 is, however, much larger than that found in L1544 (∼10000 au vs ∼4000 au).

We have investigated the origin of the differences observed in the behaviour of COMs between L1498 and L1544, by carrying out chemical modelling of both O-bearing and N-bearing COMs using the known physical structure of the L1498 starless core (Section 5). Our modelling results reveal that the enhancement of N-bearing COMs in the outer shells of L1498 at distances of ∼10000 au, is the expected outcome of the interplay between the gas-phase and the surface of dust grains given the flatter density radial profile of L1498 in comparison to the more evolved pre-stellar core L1544. Therefore, the different content in O-bearing and N-bearing complex organic material in starless and pre-stellar cores is a consequence not only of their physical structure but also, of their evolution.

ACKNOWLEDGMENTS

We also thank the staff at the IRAM 30m telescope for their help and support during the observations. We would like to thank M. Tafalla for sharing his NH_3 T_{kin} data results obtained toward L1498 and the dust and CH_3OH emission maps of this core shown in his paper Tafalla et al. (2006). We also acknowledge the input provided by J.C. Loison on the viable formation reactions for vinyl cyanide and the constructive comments from an anonymous referee that helped to improve the original version of the manuscript. This work is based on observations carried out under projects number 094-16 and 013-20 with the IRAM 30m telescope. IRAM is supported by INSU/CNRS (France), MPG (Germany) and IGN (Spain). I.J.-S. has received partial support from the Spanish State Research Agency (AEI) project numbers PID2019-105552RB-C41 and MDM-2017-0737 Unidad de Excelencia "María de Maeztu"- Centro de Astrobiología (CSIC-INTA), and from the Spanish National Research Council (CSIC) through the i-Link project number LINKA20353. The work by A.I.V. is supported by the Russian Ministry of Science and Higher Education via the State Assignment Contract FEUZ-2020-0038.

Facilities: IRAM 30m telescope

Software: MADCUBA (Martín et al. 2019), MONACO (Vasyunin et al. 2017)

REFERENCES

Agúndez, M., Marcelino, N., Cernicharo, J., Roueff, E., & Tafalla, M. 2019, A&A, 625A, 147A

Agúndez, M., & Wakelam, V. 2013, ChRv, 113, 8710A

Bacmann, A., Taquet, V., Faure, A., Kahane, C., & Ceccarelli, C. 2012, A&A, 541, L12

Balucani, N., Ceccarelli, C., & Taquet, V. 2015, MNRAS, 449, L16

Belloche, A., Müller, H., Menten, K., Schilke, P. & Comito, C. 2013, A&A, 559A, 47B

Belloche, A., et al. 2008, A&A, 482, 179B

Bizzocchi, L., Caselli, P., Spezzano, S., & Leonardo, E. 2014, A&A, 569A, 27B

Bohlin, R. C., Savage, B. D., & Drake, J. F. 1978, ApJ, 224, 132B

Bottinelli, S., et al. 2004, ApJ, 615, 354B

Caselli, P., Walmsley, C. M., Zucconi, A., Tafalla, M., Dore, L., & Myers, P. C. 2002, ApJ, 565, 331C

Cernicharo, J., Marcelino, N., Roueff, E., Gerin, M., Jiménez-Escobar, A., Muñoz Caro, G. M. 2012, ApJ, 759L, 43C

Chacón-Tanarro, A., et al. 2019, A&A, 623A, 118C

Charnley, S. B., Kress, M. E., Tielens, A. G. G. M., & Millar, T. J. 1995, ApJ, 448, 232C

Chuang, K. -J., Fedoseev, G., Qasim, D., Ioppolo, S., van Dishoeck, E. F., & Linnartz, H. 2018, ApJ, 853, 102C

Chuang, K.-J., Fedoseev, G., Ioppolo, S., van Dishoeck, E. F., & Linnartz, H. 2016, MNRAS, 455, 1702

Crapsi, A., et al., 2005, ApJ, 619, 379C

Dartois, E., Chabot, M., Bacmann, A., Boduch, P., Domaracka, A., & Rothard, H. 2020, A&A, 634A, 103D

Dartois, E., et al. 2019, A&A, 627A, 55D

Endres, C. P., Schlemmer, S., Schilke, P., Stutzki, J., & Müller, H. S. P. 2016, Journal of Molecular Spectroscopy, 327, 95

Fedoseev, G., Sciré, C., Baratta, G. A., & Palumbo, M. E. 2018, MNRAS, 475, 1819F

Fredon, A., & Cuppen, H. M. 2018, PCCP, 20, 5569F

Friberg, P., Hjalmarson, A., Madden, S. C., & Irvine, W. M. 1988, A&A, 195, 281

Galli, P. A. B., et al. 2019, A&A, 630A, 137G

Garrod, R. T., Belloche, A., Müller, H. S. P., & Menten, K. M. 2017, A&A, 601A, 48G

Garrod, R. T., Weaver, S. L. W., & Herbst, E. 2008, ApJ, 682, 283

Garrod, R. T., Wakelam, V., & Herbst, E. 2007, A&A, 467, 1103G

Harju, J., et al. 2020, ApJ, 895, 101H

Hasegawa, T. I., & Herbst, E. 1993, MNRAS, 263, 589H

Herbst, E., & van Dishoeck, E. F. 2009, ARA&A, 47, 427H

Hickson, K. M., Wakelam, V., & Loison, J.-C. 2016, MolAs, 3, 1H

Holdship, J., et al. 2019, ApJ, 880, 138H

Hollis, J. M., Lovas, F. J., Remijan, A. J., Jewell, P. R., Ilyushin, V. V., & Kleiner, I. 2006, ApJ, 643L, 25H

Hollis, J. M., Lovas, F. J., & Jewell, P. R. 2000, ApJ, 540L, 107H

Ivlev, A. V., Röcker, T. B., Vasyunin, A., & Caselli, P. 2015, ApJ, ApJ, 805, 59

Jiménez-Serra, I., et al., 2016, ApJ, 830L, 6J

Jin, M., & Garrod, R. T. 2020, ApJS, accepted. arXiv:2006.11127

Jorgensen, J. K., Favre, C., Bisschop, S. E., Bourke, T. L., van Dishoeck, E. F., & Schmalzl, M. 2012, ApJ, 757L, 4J

Lattanzi, V., et al. 2020, A&A, 633A, 118L

Marcelino, N., Cernicharo, J., Agúndez, M., et al. 2007, ApJ, 665, L127

Martín, S., Martín-Pintado, J., Blanco-Sánchez, C., Rivilla, V. M., Rodríguez-Franco, A., & Rico-Villas, F. 2019, A&A, 631A, 159M

Minissale, M., Moudens, A., Baouche, S., Chaabouni, H., & Dulieu, F. 2016, MNRAS, 458, 2953M

T. Nguyen1, S. Baouche1, E. Congiu1, S. Diana1, L. Pagani2 and F. Dulieu1

Öberg, K. I., Bottinelli, S., Jorgensen, J. K., & van Dishoeck, E. F. 2010, ApJ, 716, 825O

Pickett, H. M., Poynter, R. L., Cohen, E. A., et al. 1998, JQSRT, 60, 883

Punanova, A., et al. 2018, ApJ, 855, 112P

Quénard, D., Jiménez-Serra, I., Viti, S., Holdship, J., & Coutens, A. 2018, MNRAS, 474, 2796Q

Redaelli, E., Bizzocchi, L., Caselli, P., Sipilä, O., Lattanzi, V., Giuliano, B. M., & Spezzano, S. 2019, A&A, 629A, 15R

Rawlings, J. M. C., Williams, D. A., Viti, S., & Cecchi-Pestellini, C. 2013, MNRAS, 430, 264

Ruaud, M., Loison, J. C., Hickson, K. M., Gratier, P., Hersant, F., & Wakelam, V. 2015, MNRAS, 447, 4004R

Scibelli, S., & Shirley, Y. 2020, ApJ, 891, 73S

Shingledecker, C. N., Tennis, J., Le Gal, R., & Herbst, E. 2018, ApJ, 861, 20S

Soma, T., Sakai, N., Watanabe, Y., & Yamamoto, S. 2018, ApJ, 854, 116S

Spezzano, S., Caselli, P., Bizzocchi, L., Giuliano, B. M., & Lattanzi, V. 2017, A&A, 606A, 82S

Spezzano, S., Bizzocchi, L., Caselli, P., Harju, J., & Brünken, S. 2016, A&A, 592, L11

Tafalla, M., Myers, P. C., Caselli, P., Walmsley, C. M., & Comito, C. 2002, ApJ, 569, 815T

Tafalla, M., Myers, P. C., Caselli, P., & Walmsley, C. M. 2004, Ap&SS, 292, 347T

Tafalla, M., Santiago-García, J., Myers, P. C., Caselli, P., Walmsley, C. M., & Crapsi, A. 2006, A&A, 455, 577T

Van der Tak, F.F.S., Black, J.H., Schöier, F.L., Jansen, D.J., van Dishoeck, E.F. 2007, A&A, 468, 627

Vastel, C., Loison, J. C., Wakelam, V., & Lefloch, B. 2019, A&A, 625A, 91V

Vastel, C., Ceccarelli, C., Lefloch, B., & Bachiller, R. 2014, ApJ, 795L, 2V

Vasyunin, A. I., Caselli, P., Dulieu, F., & Jiménez-Serra, I. 2017, ApJ, 842, 33V

Vasyunin, A. I., & Herbst, E. 2013, ApJ, 769, 34

Wakelam, V., & Herbst, E. 2008, ApJ, 680, 371W

Watanabe, N., & Kouchi, A. 2002, ApJ, 571L, 173W

Willis, E. R. et al. 2020, A&A, 636A, 29W

Wirström, E. S., et al. 2011, A&A, 533A, 24W

Yoshida, K., et al. 2019, PASJ, 71S, 18Y